Diverse calcium dynamics underlie place field formation in hippocampal CA1 pyramidal cells

Mate Sumegi[1], Gaspar Olah[1], Istvan Paul Lukacs[1], Martin Blazsek[2,3], Judit K. Makara[2*] and Zoltan Nusser[1*]

[1]Laboratory of Cellular Neurophysiology, HUN-REN Institute of Experimental Medicine, Budapest, 1083, Hungary

[2] Laboratory of Neuronal Signalling, HUN-REN Institute of Experimental Medicine, Budapest, 1083, Hungary

[3] Doctoral School of Peter Pazmány Catholic University, Budapest, 1083, Hungary

* Corresponding authors: nusser@koki.hu (Z.N.) or makara.judit@koki.hun-ren.hu (J.K.M.)

Number of figures: 5

Abstract

Every explored environment is represented in the hippocampus by the activity of distinct populations of pyramidal cells (PCs) that typically fire at specific locations called their place fields (PFs). PFs are constantly born even in familiar surroundings (during representational drift), and many rapidly emerge when the animal explores a new or altered environment (during global or partial remapping). Behavioral time scale synaptic plasticity (BTSP), a plasticity mechanism based on prolonged somatic bursts induced by dendritic Ca^{2+} plateau potentials, was recently proposed as the main cellular mechanism underlying new PF formations (PFF), but it is unknown whether burst-associated large somatic [Ca^{2+}] transients are necessary and/or sufficient for PFF. To address this issue, here we performed *in vivo* two-photon [Ca^{2+}] imaging of hippocampal CA1 PCs in head-restrained mice to investigate somatic [Ca^{2+}] dynamics underlying PFFs in familiar and novel virtual environments. Our results demonstrate that although many PFs are formed by BTSP-like events, PFs also frequently emerge with initial [Ca^{2+}] dynamics that do not match any of the characteristics of BTSP. BTSP and non-BTSP-like new PFFs occur spontaneously in familiar environments, during neuronal representational switches and instantaneously in new environments. Our data also reveal that solitary [Ca^{2+}] transients that exceed in amplitude those evoking BTSP-like PFFs frequently occur without inducing PFs, demonstrating that large [Ca^{2+}] transients *per se* are not sufficient for PFF.

Introduction

The hippocampus plays a critical role in spatial and contextual memory processes by forming cognitive maps of environments (Lisman et al., 2017; Moser et al., 2008; O'Keefe and Dostrovsky, 1971) that can support effective navigation towards learned salient locations (Robinson et al., 2020). During navigation many pyramidal cells (PCs) in the dorsal hippocampal CA1 area (CA1PCs) exhibit action potential (AP) firing that is restricted to spatial locations, the cell's place fields (PFs). In different environments the activity of CA1PCs reorganizes to collectively form distinct representations, i.e. creating specific maps of each environment. In a novel environment, some CA1PCs are active already during the first traversal of their PFs, but many cells become place cells after some delay (Dong et al., 2021). Furthermore, spatial maps also gradually reorganize during continuous or repeated exploration in already familiar environments due to changes in the activity of individual PCs, including the recruitment of new place cells into the representation (Dong et al., 2021; Keinath et al., 2022; Mankin et al., 2012; Rubin et al., 2015; Ziv et al., 2013). Despite the fundamental importance of the dynamic hippocampal population code in spatial navigation, the mechanisms initiating and mediating new PF formations (PFFs) are still poorly understood.

How can place cells acquire their PFs? While cells that are already active at the first traversal of their PFs may simply receive sufficient active synaptic inputs *ab ovo*, delayed PFF is assumed to require dynamic changes in synaptic inputs to or the intrinsic excitability of CA1PCs. The cellular mechanisms underlying *de novo* formation of PFs have been elusive due to difficulties in measuring the subthreshold activity pattern that drives AP firing. However, recent studies have shed light on possible mechanisms. Most strikingly, *in vivo* patch-clamp recordings in head-fixed mice running on a familiar cue-rich treadmill revealed the spontaneous appearance of new PFs in previously silent cells, following the sudden occurrence of a robust, prolonged depolarization driving complex spike burst (CSB) firing (Bittner et al., 2015). Such CSBs are thought to be driven by dendritic Ca^{2+} spikes (plateau potentials) mediated by voltage-gated Ca^{2+} channels and NMDA receptors (Grienberger et al., 2014; Takahashi and Magee, 2009). The formation of new PFs by plateau potentials is thought to be mediated by synaptic plasticity obeying a non-Hebbian rule, whereby the excitatory input synapses activated in a ~2-second-long time window around the CSB are rapidly potentiated. This form of plasticity was named behavioral time scale synaptic plasticity (BTSP; Bittner et al., 2017; Milstein et al., 2021). After initial electrophysiological demonstration, spontaneous PFF with BTSP-like characteristics was observed in CA1PCs by *in vivo* [Ca^{2+}] imaging as well (Adoff et al., 2021;

Grienberger and Magee, 2022; Priestley et al., 2022; Rolotti et al., 2022). Confirming the mechanism, PFF with features similar to spontaneous BTSP-like PFF could also be induced artificially by strong sustained electrical or optical depolarization of a cell, a stimulus assumed to evoke Ca^{2+} plateau potentials (Bittner et al., 2015; Bittner et al., 2017; Diamantaki et al., 2018; Fan et al., 2023; Milstein et al., 2021; Rolotti et al., 2022). In summary, BTSP evoked by CSBs has been proposed to serve as the main mechanism driving *de novo* PFF; however, its triggering mechanisms are enigmatic and its prevalence under different behavioral conditions is not yet known.

Whereas BTSP is a suitable and attractive candidate, other mechanisms may also contribute to PFF. *In vivo* patch-clamp recordings by Cohen et al. (2017) from CA1PCs in head-fixed mice running in a novel virtual environment showed that most of the delayed PFFs did not begin with CSBs, but with a weak subthreshold spatially tuned depolarization. This result suggests the involvement of synaptic plasticity mechanisms other than BTSP, such as e.g. spike timing dependent plasticity (STDP; Bi and Poo, 1998; Magee and Johnston, 1997; Markram et al., 1997) or cooperative plasticity mechanisms operating locally in dendrites (Golding et al., 2002; Kim et al., 2015; Mago et al., 2020). Furthermore, network mechanisms may also drive the emergence of new PFs. It has been shown that optogenetic stimulation of a small subset of CA1PCs at a particular location induced persistent PFF or remapping in non-stimulated cells, suggesting that changes in synaptic coupling and circuit dynamics of PCs and inhibitory interneurons can also lead to reorganization of spatial maps by unmasking latent PFs (McKenzie et al., 2021). Also pointing to a network effect, optical induction of BTSP-like PFF has been shown to be restricted by lateral inhibition, strongly limiting the number of CA1PCs that can simultaneously form new PFs by BTSP (Rolotti et al., 2022). Altogether, a comprehensive understanding of the contribution of possibly diverse cellular mechanisms underlying PFF during various forms of remapping processes is lacking. BTSP has several unique features when probed by somatic [Ca^{2+}] imaging (Grienberger and Magee, 2022; Priestley et al., 2022). First, the prolonged CSB results in large [Ca^{2+}] transient during the initial PFF event, typically followed by weaker Ca^{2+} signals on consecutive traversals through the PF. Second, due to the long and asymmetric temporal kernel of the plasticity (favoring potentiation of inputs active 1-2 seconds before the CSB) a substantial backward shift in the spatial position of the PF center can be observed on linear tracks after the formation lap. Third, the width of the new PF is generally proportional to the running speed of the animal during the PFF event. In contrast, PFF by other synaptic or network mechanisms is not expected to exhibit such properties. Using these features, we aimed to characterize PFFs as mediated by BTSP- or non-BTSP-like mechanisms in large populations of

107 CA1PCs. We performed two-photon [Ca^{2+}] imaging of CA1PCs in head-fixed mice performing a
108 spatial navigation task in familiar and partially novel virtual corridors. We find that BTSP is prevalent
109 but is not the only mechanism driving PFFs, as many new PFs formed without exhibiting any of the
110 characteristics of BTSP. Furthermore, we show that robust CSB-like somatic activity is often
111 ineffective in inducing new PFFs, suggesting that additional factors are required than just CSBs to
112 successfully initiate new PFs.

113

114 **Results**

115 **Place modulated activity of CA1PCs in mice navigating in a virtual corridor**

116 *In vivo* two-photon [Ca^{2+}] imaging of CA1PCs was performed from the dorsal hippocampus of
117 head-restrained double transgenic mice (Thy1-GCaMP6s and Cre-dependent td-Tomato), injected
118 with diluted Cre-recombinase expressing AAV (Figure 1A-B). Mice were trained to run in an ~8-
119 meter-long virtual corridor for a water reward. The wall of the virtual corridor contained 6 well-
120 discernable visual landmarks, the last of which indicated the reward zone, where mice were required
121 to lick for water reward (Figure 1C). Well-trained mice ran with a relatively constant speed of ~30-
122 40 cm / s through the corridor and slowed down and started licking just before entering the reward
123 zone (Figure 1D), indicating that they learned the position of the reward zone. Imaging was
124 performed in well-trained mice across multiple days (n = 163 imaging sessions of 45 mice). The
125 imaging field of view contained ~500-1000 CA1PC somata (Figure 1B), which showed highly
126 variable activities during the session (Figure 1E - H); some cells were silent whereas others showed
127 moderate to high activity rates. Plotting the activity as a function of the animal's location in the
128 virtual corridor showed high variability in the spatial tuning of active cells (Figure 1I, for PF
129 determination see Methods). The PFs of place cells tiled the entire length of the corridor with
130 enrichments around the visual landmarks (Figure 1J). Place cells had variable number of PFs with
131 widely different widths, covering a variable fraction of the virtual corridor (Figure 1K). These results
132 demonstrate that the activity of CA1PCs in our experimental conditions is comparable to that
133 observed in freely moving animals exploring large environments (Eliav et al., 2021; Lee et al., 2020;
134 Rich et al., 2014).

135 **BTSP and non-BTSP-like mechanisms are both prevalent PFF mechanisms**

During navigation in the familiar virtual corridor, new PFs often appeared suddenly at various spatial locations during the session (Figures 2, 3). To investigate the possible mechanisms underlying such a robust change of activity, we examined the dynamics of the newly formed PFs. If BTSP is the mechanism generating new PFs in CA1PCs, the PFs are expected to have the following characteristics: first, since BTSP is induced by a Ca^{2+} plateau potential and consequential prolonged CSB (Bittner et al., 2015), we expect that the amplitude of the [Ca^{2+}] transient in the formation lap is larger than that in the following laps. Second, because of the asymmetrical temporal kernel of BTSP (Bittner et al., 2017), the center of mass (COM) of the new PF is expected to shift to the backward direction compared to the peak activity in the formation lap. To quantify these dynamics, we calculated two parameters for each newly formed PF: the formation lap gain and the initial COM shift (see Methods and Priestley et al., 2022). We then categorized all newly formed PFs in our recordings based on these two parameters. Using a conservative approach, we categorized a new PF to be formed by a BTSP-like mechanism if it had both positive gain and negative shift values (Figure 2A; n = 310 new PFs), whereas new PFs exhibiting neither positive gain nor negative shift were considered as non-BTSP-like events (Figure 2B; n = 59). All other newly formed PFs (no-gain with backward shift and gain without backward shift) were excluded from further analysis. This analysis thus demonstrated that, whereas a large fraction of newly formed PFs were generated by a BTSP-like mechanism, a substantial fraction of new PFF was produced by a different process.

Comparison of the [Ca^{2+}] transients of BTSP-like (n = 310) and non-BTSP-like (n = 59) new PFs in the laps before, during and after their formation showed that, apart from the strongly different [Ca^{2+}] signal amplitudes in the formation lap, [Ca^{2+}] transients within the PF on the subsequent laps had similar amplitudes (Figure 2C) and ratios of active laps (0.86 ± 0.03 vs. 0.86 ± 0.06), indicating that the basic characteristics of activity in the stabilized new PFs were comparable between the two groups. Furthermore, both types of new PFs exhibited similar distributions along the virtual track, tiling the whole corridor with enrichments around the visual landmarks (Figure 3A).

A further characteristic feature of the BTSP mechanism is that, due to its seconds-wide temporal kernel, the width of the new PF is proportional to the running speed of the animal during the formation lap, i.e. the potentiated inputs cover a wider spatial sector if the animal travels longer distance during the plasticity time window (Bittner et al., 2017). As an independent confirmation that newly formed PFs in our categorization of PF groups genuinely differed in the mechanisms underlying their formation, we found a significant positive correlation between formation lap

running speed and PF width in the BTSP-like but not in the non-BTSP-like PF category (Figure 3B). Because of the difference in the number of events in the two groups, we randomly subsampled the BTSP-like events to the sample size of the non-BTSP-like PFF events 10 000 times and performed regression analysis. This bootstrapping revealed that both the r and p values of the fit to the non-BTSP data fall outside the 95% confidence interval of the bootstrapped BTSP values, therefore we conclude that the lack of significant correlation between the running speed and the PF width for the non-BTSP-like events is not the consequence of the smaller sample size.

Concentrated PFF associated with representational switch

We next examined the distribution of new PFF events across imaging sessions and laps. While in most of the sessions the number of newly formed PFs was moderate, few sessions contained an unusually large number of such events (Figure 3C). When we examined the distribution of new PFFs in these sessions across individual laps, we found that the majority of PFF events occurred within a short period over a limited number (3-10) of consecutive laps (Figure 3D). These concentrated PFF periods were termed as PFF 'surges', which included PFs formed both by BTSP- and non-BTSP-like mechanisms (non-BTSP / BTSP ratio: 0.57). The unusually high rate of new PFF events during PFF surges led us to investigate whether they were associated with a more general network-wide reorganization of the CA1PC representation of the virtual corridor. Indeed, we found that the lap-by-lap correlation of activity in the whole population of imaged CA1PCs underwent a drastic and rapid switch between two stable states before and after the PFF surge. A closer look indicated that the initial representation began to disorganize as the surge started to ramp up, and a new coherent representation started at the lap with the peak PFF rate. In contrast, no such representational switches were observed in sessions without PFF surges (Figure 3D bottom). Finally, when we compared the [Ca^{2+}] dynamics of PFFs during surges with those of PFF outside the surges, we found similar [Ca^{2+}] amplitudes in both the BTSP-like and non-BTSP-like groups, except for higher Ca^{2+} signals in the first lap after the formation lap in the non-BTSP group during surges compared to outside surges (Figure 3E). The period including the PFF surge and representational switch was not accompanied by any noticeable change in the behavior of the animals as assessed by running speed and lick rate. Altogether these results reveal unique, short epochs during task-engaged behavior when rapid reorganization of the population activity of CA1PCs occurs, in part due to new PFFs by both BTSP- and non-BTSP-like mechanisms.

New PFF in a novel environment is mediated by both BTSP- and non-BTSP-like mechanisms

CA1PCs are known to rapidly remap in novel environments to create a specific representation of newly explored locations. We next sought to determine the contribution of BTSP- and non-BTSP-like mechanisms to new PFFs in a novel environment by extending the familiar virtual corridor with a 6-m-long segment decorated with never-seen visual landmarks during the imaging session. Animals traversed this novel segment with an average speed comparable to that in the familiar portion of the maze. The maze extension did not induce a detectable change in lick frequency. At the end of the familiar segment of the 14-meter-long corridor, the animals reduced their running speed and displayed anticipatory licking just before entering the reward zone similar to their performance in the standard 8-meter-long corridor. Population-level analysis revealed a reorganization of the neuronal representation, as demonstrated by a decreased population vector correlation between the extended and original maze, despite high intra-segment correlations (mean correlation coefficients: original maze odd vs. even: 0.50±0.21, original maze odd vs. extended maze even: 0.08±0.06, extended maze odd vs even: 0.36±0.12; n = 6 mice; Repeated Measures ANOVA followed by Tukey *post hoc* test: original maze odd-even vs. original maze odd - extended maze even: $p < 0.001$, extended maze odd - even vs. original maze odd - extended maze even: $p = 0.002$, original maze odd - even vs. extended maze odd - even: $p = 0.114$). Consistent with previous studies (Dong et al., 2021; Priestley et al., 2022; Sheffield et al., 2017), we observed many new PFs already during the first traversal in the novel virtual environment, and additional new PFs formed during subsequent laps, although with lower probability (Figure 4A, B). The frequency of new PFFs was the highest in the first few laps for both BTSP- and non-BTSP-like events. Analyzing the somatic [Ca^{2+}] transients revealed that their amplitudes were very similar to those observed in the familiar environment for both the BTSP- and non-BTSP-like PFF events during the 1st traversal (Figure 4C). Interestingly, the relative prevalence of non-BTSP-like PFF was higher in the first laps of the novel environment than that observed in the familiar environments (novel corridor lap 1-2: n = 24 non-BTSP, n = 44 BTSP in 6 mice, non-BTSP/BTSP ratio = 0.55; familiar corridor: n = 59 non-BTSP, n = 310 BTSP in 30 mice, non-BTSP/BTSP ratio = 0.19; Chi-square test: $p < 0.001$), whereas in the subsequent laps BTSP-like PFF dominated again (novel corridor region, laps 3-31: non-BTSP / BTSP ratio = 0.16).

Large somatic [Ca^{2+}] transients *per se* are not sufficient to induce new PFs

227 The above analysis demonstrated an important role for BTSP in new PF formations; however, it
228 also indicated that BTSP is not an exclusive mechanism of PFF, as new PFs could also develop
229 rather gradually without strong initial somatic activity during the formation lap. Finally, we asked the
230 question in reverse: is the occurrence of strong somatic Ca^{2+} activity sufficient to trigger the
231 formation of new PFs? To address this, we selected CA1PCs exhibiting at least one BTSP-like newly
232 formed PF in a given imaging session in the familiar corridor and identified all somatic Ca^{2+}
233 transients in that session that had amplitudes larger than the Ca^{2+} transient initiating the BTSP-like
234 PFF event (if multiple PFs were formed then the largest formation lap [Ca^{2+}] transient was used;
235 Figure 5). We found that, in approximately one quarter of the sessions, BTSP-inducing [Ca^{2+}]
236 transients could be matched with at least one larger [Ca^{2+}] transient that failed to initiate new PFF
237 ('solitary events', Figure 5A - B). Our results together suggest that a large somatic [Ca^{2+}] transient is
238 neither necessary nor sufficient to induce the formation of new PFs.

239

240 **Discussion**

241 In the present study we performed *in vivo* two-photon [Ca^{2+}] imaging from hundreds of dorsal
242 hippocampal CA1PCs while mice ran for a water reward in a familiar and a partially novel virtual
243 environment. During the exploration of familiar and novel corridors, PFF events occurred in
244 CA1PCs spontaneously along the entire corridor. Many of these events had characteristics
245 reminiscent to those reported earlier for BTSP-like PFF events, but a significant fraction of PPFs
246 had small [Ca^{2+}] transient amplitudes in the formation lap and did not show the characteristic
247 backward shift in the COM of the newly formed PF. Such non-BTSP-like PFs not only occurred
248 spontaneously in the familiar environment but were also formed during representational switches
249 within familiar and in the first laps of a novel environment. We also observed that in many
250 behavioral sessions when a CA1PC displayed a BTSP-like PFF event, there were [Ca^{2+}] transients
251 ('solitary events') with amplitudes higher than that of the formation lap of the BTSP-like PFF event,
252 which did not induce novel PFs. These results demonstrate that BTSP-like PFFs are not the only
253 mechanisms of new PFFs and that large somatic [Ca^{2+}] transients are not sufficient *per se* to induce
254 new PFs.

255 The lack of large initial somatic [Ca^{2+}] transients – that are likely associated with strong bursts
256 involving Ca^{2+} plateaus - during non-BTSP-like PFFs suggests two possible scenarios: they either do
257 not involve excitatory synaptic plasticity in CA1PCs but rather result from a change of incoming

258 excitatory or inhibitory synaptic inputs, or they are driven by other synaptic plasticity mechanisms
259 that do not require global Ca^{2+} plateaus and CSBs to increase excitatory synaptic weights. Local
260 synaptic plasticity in individual dendritic branches is a particularly intriguing possibility for the latter
261 scenario, since it has been shown that PFF can be preceded by local dendritic activity in the future
262 PF locations (Sheffield et al., 2017). This activity, presumably produced by clustered activation of
263 Schaffer collateral synapses (Adoff et al., 2021) may induce local synaptic potentiation, whereby the
264 inputs eventually become suprathreshold at the soma manifesting as non-BTSP-like PFF.
265 Importantly, long-term potentiation (LTP) of excitatory synaptic inputs by local dendritic Na^{+}
266 and/or NMDA spikes (d-spikes) can be induced by a single or a few repetitions of d-spikes (Mago
267 et al., 2020; Remy and Spruston, 2007), and thus can be consistent with rapid generation of new PFs
268 similar to BTSP. It remains to be explored whether the temporal coincidence kernel of local d-spike-
269 induced LTP is on millisecond or second time scales, i.e. different or similar to that of BTSP. In
270 contrast to synaptic plasticity induced by d-spikes, LTP induced by cooperative activity of clustered
271 excitatory inputs without evoking APs or d-spikes (Mago et al., 2020) or LTP induced by STDP (Bi
272 and Poo, 1998; Magee and Johnston, 1997; Markram et al., 1997) require larger number of repeated
273 co-activations of pre- and postsynaptic cells and thus may be incompatible with fast PFF and global
274 remapping. However, it cannot be ruled out that non-BTSP-like PFFs occurring after many
275 traversals of the same location in familiar environments may involve STDP. Furthermore, since
276 STDP in CA1PCs has been characterized under *in vitro* conditions, it is yet unknown whether its
277 induction rules are similar *in vivo*, especially in the presence of active neuromodulatory systems,
278 which may act as a reinforcement signal to influence STDP rules even at synapses with temporally
279 distant activity *via* presumed eligibility traces (e.g. Fisher et al., 2017).

280 By showing that both BTSP- and non-BTSP-like PFFs can underlie changes in spatial tuning of
281 CA1PCs and by dissecting their relative contribution under different remapping conditions, our
282 study reconciles diverse and sometimes contradictory earlier observations. Although BTSP-like PFF
283 events have been suggested recently as a dominant mechanism of new PFFs in the hippocampus
284 (Bittner et al., 2015; Bittner et al., 2017; Grienberger and Magee, 2022; Milstein et al., 2021; Rolotti et
285 al., 2022), previous results also indicated that PFs in a new environment frequently form without
286 CSBs (Cohen et al., 2017). Recording from a large number of CA1PCs, we could estimate the
287 prevalence of BTSP-like and non-BTSP-like PFFs during various forms of remapping (although we
288 note that our estimates likely underrepresent non-BTSP-like PFF due to the limited sensitivity of the
289 genetically encoded Ca^{2+} indicator to detect few APs). We found that BTSP dominates PFFs under

290 conditions when new PFs are born in individual CA1PCs that are part of a relatively stable
291 representation in a familiar environment, i.e. during gradual representational drift. On the contrary,
292 the relative ratio of non-BTSP-like PFF was much higher in the first laps of running in a novel
293 corridor segment. This may be consistent with a global remapping process in response to
294 reconfiguration of the excitatory input patterns arriving to individual CA1PCs from upstream areas.
295 As a result, in some CA1PCs no plasticity would be required to immediately generate a new PF,
296 while in other CA1PCs plasticity of the newly activated inputs (e.g. by activating local d-spikes) may
297 also contribute to non-BTSP-like PFF, with this process possibly facilitated by a change in brain
298 state due to the novelty of the new corridor segment. These processes altogether could increase the
299 contribution of non-BTSP-like PFF to the initial development of the novel representation of the
300 newly explored corridor.

301 Our results are consistent with previous reports of increased PFF during initial exposure to novel
302 environments (Priestley et al., 2022) and around newly introduced salient cues in a familiar
303 environment (Grienberger and Magee, 2022), although certain differences may be apparent. In
304 particular, Priestley et al (2022), who classified BTSPs similarly to our method but pooled all PFF
305 events not clearly BTSP as an 'other' group, observed increased fraction of BTSP-like PFF on the
306 first trial in a novel environment compared to a familiar environment (Priestley et al., 2022). Here,
307 however, we have found an increase in the prevalence of non-BTSP-like PFF events during the
308 initial exposure to the novel corridor. Yet, these results are not directly comparable for the following
309 reasons: first, we defined the non-BTSP-like group as a subclass of 'other' PFFs based on multiple
310 feature criteria to clearly separate them from BTSP-like PFFs; second, in the familiar environment
311 we only analyzed PFs that were formed newly after an silent period in at least 16 laps, whereas
312 (Priestley et al., 2022) analyzed all PFs including those with established activity from the first lap in
313 an environment.

314 Interestingly, we also observed spontaneous surges of coordinated new PFF events during short
315 imaging epochs involving a few laps in the familiar corridor. These PFF surges included a high
316 fraction of both non-BTSP- and BTSP-like PFF events, and were associated with global remapping
317 of the CA1 representation. The precise trigger and relevance of these representational 'switches' in
318 a well-learned, invariant environment is currently unknown, but we speculate that – in the absence
319 of alterations of sensory cues and task demands – they may indicate a change in the internal state of
320 the animal, or a transition between relying on different signals for navigation (e.g. sensory cues vs

self-motion), assigning distinct internal contexts to the same environment (Sanders et al., 2020). Although different CA1 population codes across subsequent (interrupted) explorations of the same maze have been demonstrated (Sheintuch et al., 2020), to our knowledge similar representational switches during a continuous behavioral epoch in an unchanged environment have only been described in the entorhinal cortex (EC; Low et al., 2021). It is possible that the representation switches we observed originate in the EC, which thus provides globally remapped inputs to the hippocampus similarly to the situation in a novel corridor. Overall, the higher ratio of non-BTSP-like PFFs in the initial laps of the novel environment and during representational switches (both ~0.55) than that in the familiar environment (0.19) suggests that distinct cellular/synaptic mechanisms might contribute to gradual representational drifts and abrupt global remapping.

While sudden large Ca^{2+} activity at a location where a cell was previously inactive could often induce BTSP-like PFF, our results also demonstrate that a large fraction of even stronger Ca^{2+} activities failed to initiate PFF in the same cell. If we assume that the large (and often prolonged) somatic Ca^{2+} signals represent CSBs, this indicates either that the synaptic plasticity induced by the underlying plateau was not sufficiently strong to evoke somatic firing, or that the induction of plasticity may be gated by additional conditional factor(s), for example modulatory signals or inhibition. This latter possibility highlights the importance of elucidating the molecular components contributing to the initiation, expression and regulatory mechanisms governing the long-term increase in synaptic strength by BTSP. While research efforts of the past three-four decades provided an enormous amount of information regarding the molecular mechanisms underlying Hebbian synaptic plasticity, the molecular events taking place during BTSP are almost completely unknown. Further research will be crucial to reveal the similarities and differences in the molecular mechanisms underlying these fundamentally different synaptic plasticities, which will allow us to design molecular modifications that specifically alter only one of them to uncover its consequences on new PFFs and animal behaviors.

Acknowledgements

ZN is the recipient of a European Research Council Advanced Grant (ERC-AG 787157). JKM is supported by a European Research Council Consolidator Grant (ERC-CoG 771849) and the International Research Scholar Program of the Howard Hughes Medical Institute (55008740). The work of JKM and ZN is supported by the National Brain Research Program (NAP 3.0) of the Hungarian Academy of Sciences (NAP2022-I-1/2022). The financial support from these funding bodies is gratefully acknowledged.

Author Contributions

MS, GO, IPL, ZN designed the experiments; GO, IPL, MS performed the *in vivo* imaging experiments, MB developed analysis of PF categories; MS developed analysis tools and analyzed the data guided by ZN and JKM; MS, JKM, ZN wrote the manuscript.

Declaration of Interest

The authors declare no competing interests.

364 **References**

365 Adoff, M.D., Climer, J.R., Davoudi, H., Marvin, J.S., Looger, L.L., and Dombeck, D.A. (2021). The
366 functional organization of excitatory synaptic input to place cells. Nature communications *12*, 3558.

367 Bi, G., and Poo, M. (1998). Synaptic modifications in cultured hippocampal neurons: dependence on
368 spike timing, synaptic strength, and postsynaptic cell type. J Neurosci *18*, 10464-10472.

369 Bittner, K.C., Grienberger, C., Vaidya, S.P., Milstein, A.D., Macklin, J.J., Suh, J., Tonegawa, S., and
370 Magee, J.C. (2015). Conjunctive input processing drives feature selectivity in hippocampal CA1
371 neurons. Nature neuroscience *18*, 1133-1142.

372 Bittner, K.C., Milstein, A.D., Grienberger, C., Romani, S., and Magee, J.C. (2017). Behavioral time
373 scale synaptic plasticity underlies CA1 place fields. Science (New York, NY *357*, 1033-1036.

374 Cohen, J.D., Bolstad, M., and Lee, A.K. (2017). Experience-dependent shaping of hippocampal CA1
375 intracellular activity in novel and familiar environments. eLife *6*.

376 Diamantaki, M., Coletta, S., Nasr, K., Zeraati, R., Laturnus, S., Berens, P., Preston-Ferrer, P., and
377 Burgalossi, A. (2018). Manipulating Hippocampal Place Cell Activity by Single-Cell Stimulation in
378 Freely Moving Mice. Cell Rep *23*, 32-38.

379 Dong, C., Madar, A.D., and Sheffield, M.E.J. (2021). Distinct place cell dynamics in CA1 and CA3
380 encode experience in new environments. Nature communications *12*, 2977.

381 Eliav, T., Maimon, S.R., Aljadeff, J., Tsodyks, M., Ginosar, G., Las, L., and Ulanovsky, N. (2021).
382 Multiscale representation of very large environments in the hippocampus of flying bats. Science
383 (New York, NY *372*.

384 Fan, L.Z., Kim, D.K., Jennings, J.H., Tian, H., Wang, P.Y., Ramakrishnan, C., Randles, S., Sun, Y.,
385 Thadhani, E., Kim, Y.S.*, et al.* (2023). All-optical physiology resolves a synaptic basis for behavioral
386 timescale plasticity. Cell *186*, 543-559 e519.

387 Fisher, S.D., Robertson, P.B., Black, M.J., Redgrave, P., Sagar, M.A., Abraham, W.C., and Reynolds,
388 J.N.J. (2017). Reinforcement determines the timing dependence of corticostriatal synaptic plasticity
389 in vivo. Nature communications *8*, 334.

390 Golding, N.L., Staff, N.P., and Spruston, N. (2002). Dendritic spikes as a mechanism for cooperative
391 long-term potentiation. Nature *418*, 326-331.

392 Grienberger, C., Chen, X., and Konnerth, A. (2014). NMDA receptor-dependent multidendrite
393 Ca(2+) spikes required for hippocampal burst firing in vivo. Neuron *81*, 1274-1281.

394 Grienberger, C., and Magee, J.C. (2022). Entorhinal cortex directs learning-related changes in CA1
395 representations. Nature *611*, 554-562.

396 Keinath, A.T., Mosser, C.A., and Brandon, M.P. (2022). The representation of context in mouse
397 hippocampus is preserved despite neural drift. Nature communications *13*, 2415.

Kim, Y., Hsu, C.L., Cembrowski, M.S., Mensh, B.D., and Spruston, N. (2015). Dendritic sodium spikes are required for long-term potentiation at distal synapses on hippocampal pyramidal neurons. eLife *4*.

Lee, J.S., Briguglio, J.J., Cohen, J.D., Romani, S., and Lee, A.K. (2020). The Statistical Structure of the Hippocampal Code for Space as a Function of Time, Context, and Value. Cell *183*, 620-635 e622.

Lisman, J., Buzsaki, G., Eichenbaum, H., Nadel, L., Ranganath, C., and Redish, A.D. (2017). Viewpoints: how the hippocampus contributes to memory, navigation and cognition. Nature neuroscience *20*, 1434-1447.

Low, I.I.C., Williams, A.H., Campbell, M.G., Linderman, S.W., and Giocomo, L.M. (2021). Dynamic and reversible remapping of network representations in an unchanging environment. Neuron *109*, 2967-2980 e2911.

Magee, J.C., and Johnston, D. (1997). A synaptically controlled, associative signal for Hebbian plasticity in hippocampal neurons. Science (New York, NY *275*, 209-213.

Mago, A., Weber, J.P., Ujfalussy, B.B., and Makara, J.K. (2020). Synaptic Plasticity Depends on the Fine-Scale Input Pattern in Thin Dendrites of CA1 Pyramidal Neurons. J Neurosci *40*, 2593-2605.

Mankin, E.A., Sparks, F.T., Slayyeh, B., Sutherland, R.J., Leutgeb, S., and Leutgeb, J.K. (2012). Neuronal code for extended time in the hippocampus. Proceedings of the National Academy of Sciences of the United States of America *109*, 19462-19467.

Markram, H., Lubke, J., Frotscher, M., and Sakmann, B. (1997). Regulation of synaptic efficacy by coincidence of postsynaptic APs and EPSPs. Science (New York, NY *275*, 213-215.

McKenzie, S., Huszar, R., English, D.F., Kim, K., Christensen, F., Yoon, E., and Buzsaki, G. (2021). Preexisting hippocampal network dynamics constrain optogenetically induced place fields. Neuron *109*, 1040-1054 e1047.

Milstein, A.D., Li, Y., Bittner, K.C., Grienberger, C., Soltesz, I., Magee, J.C., and Romani, S. (2021). Bidirectional synaptic plasticity rapidly modifies hippocampal representations. eLife *10*.

Moser, E.I., Kropff, E., and Moser, M.B. (2008). Place cells, grid cells, and the brain's spatial representation system. Annual review of neuroscience *31*, 69-89.

O'Keefe, J., and Dostrovsky, J. (1971). The hippocampus as a spatial map. Preliminary evidence from unit activity in the freely-moving rat. Brain Res *34*, 171-175.

Priestley, J.B., Bowler, J.C., Rolotti, S.V., Fusi, S., and Losonczy, A. (2022). Signatures of rapid plasticity in hippocampal CA1 representations during novel experiences. Neuron *110*, 1978-1992 e1976.

Remy, S., and Spruston, N. (2007). Dendritic spikes induce single-burst long-term potentiation. Proceedings of the National Academy of Sciences of the United States of America *104*, 17192-17197.

433 Rich, P.D., Liaw, H.P., and Lee, A.K. (2014). Place cells. Large environments reveal the statistical
434 structure governing hippocampal representations. Science (New York, NY *345*, 814-817.

435 Robinson, N.T.M., Descamps, L.A.L., Russell, L.E., Buchholz, M.O., Bicknell, B.A., Antonov, G.K.,
436 Lau, J.Y.N., Nutbrown, R., Schmidt-Hieber, C., and Hausser, M. (2020). Targeted Activation of
437 Hippocampal Place Cells Drives Memory-Guided Spatial Behavior. Cell *183*, 1586-1599 e1510.

438 Rolotti, S.V., Ahmed, M.S., Szoboszlay, M., Geiller, T., Negrean, A., Blockus, H., Gonzalez, K.C.,
439 Sparks, F.T., Solis Canales, A.S., Tuttman, A.L.*, et al.* (2022). Local feedback inhibition tightly
440 controls rapid formation of hippocampal place fields. Neuron *110*, 783-794 e786.

441 Rubin, A., Geva, N., Sheintuch, L., and Ziv, Y. (2015). Hippocampal ensemble dynamics timestamp
442 events in long-term memory. eLife *4*.

443 Sanders, H., Wilson, M.A., and Gershman, S.J. (2020). Hippocampal remapping as hidden state
444 inference. eLife *9*.

445 Sheffield, M.E.J., Adoff, M.D., and Dombeck, D.A. (2017). Increased Prevalence of Calcium
446 Transients across the Dendritic Arbor during Place Field Formation. Neuron *96*, 490-504 e495.

447 Sheintuch, L., Geva, N., Baumer, H., Rechavi, Y., Rubin, A., and Ziv, Y. (2020). Multiple Maps of the
448 Same Spatial Context Can Stably Coexist in the Mouse Hippocampus. Curr Biol *30*, 1467-1476
449 e1466.

450 Skaggs, W., Mcnaughton, B., and Gothard, K. (1992). An information-theoretic approach to
451 deciphering the hippocampal code. Adv Neural Inf Process Syst *5*, 1030–1037.

452 Takahashi, H., and Magee, J.C. (2009). Pathway interactions and synaptic plasticity in the dendritic
453 tuft regions of CA1 pyramidal neurons. Neuron *62*, 102-111.

454 Ziv, Y., Burns, L.D., Cocker, E.D., Hamel, E.O., Ghosh, K.K., Kitch, L.J., El Gamal, A., and
455 Schnitzer, M.J. (2013). Long-term dynamics of CA1 hippocampal place codes. Nature neuroscience
456 *16*, 264-266.

457

458

459 **Materials and methods**

460 **Animals**

461 A total of 45 (23 male and 22 female) Ai9xGP4.3 double-transgenic mice were used in this study.
462 These animals were also involved in separate experiments unrelated to the current investigation.
463 Mice were housed in the vivarium of the HUN-REN Institute of Experimental Medicine under a
464 standard 12-hour light/dark cycle with *ad libitum* access to water and food. Water intake was
465 restricted during the experiments (details provided below). All procedures adhered to the regulations
466 outlined in the Hungarian Act of Animal Care and Experimentation (40/2013 [II.14]) and received
467 approval from the Animal Committee of the Institute of Experimental Medicine, Budapest.

468 **Virus injection**

469 Mice were first anesthetized with an intraperitoneal injection of a mixture of ketamine
470 hydrochloride (CP-ketamine, 62.5 mg/kg), xylazine (CP-Xylazine, 12.5 mg/kg), and promethazine
471 hydrochloride (Pipolphen, 6.25 mg/kg). Local anesthesia was achieved by subcutaneous injection of
472 ropivacaine hydrochloride (Naropine, 50-100 µl, 2 mg/ml). To protect the eyes, Opticorn A
473 ointment was applied. The animal's head was then fixed in a stereotaxic frame, and a craniotomy of
474 ~0.5 mm in diameter was made above the injection site. Four times 25 nl AAV vector
475 (pENN.AAV.hSyn.Cre.WPRE.hGH, 3.3 x 10^{10} GC/ml, Addgene #105553-AAV9) was injected into
476 the left hemisphere at coordinates AP: -2, DV: -1.1, ML: 1.8. with 2.3 nl/sec bouts separated by 1-
477 minute intervals. Following surgery, buprenorphine hydrochloride (Bupaq, 0.1 mg/kg) and carprofen
478 (Rimadyl, 25 mg/kg) were administered subcutaneously for analgesia and preventing inflammation.
479 Carprofen (35 ng/ml) was also supplemented in the drinking-water for the following two days of
480 postoperative care.

481 **Implant surgery**

482 After virus injection (median: 7, range: 2 to 32 days) animals were anesthetized with Isoflurane
483 (1.5% in carbogen, flow rate 0.8 l/min). A 3 mm diameter craniotomy was created over the virus
484 injection site and the cortex above the hippocampus was gently aspirated. A 3 mm diameter 1.7 mm
485 long stainless-steel cannula with a glass coverslip attached to the bottom was inserted and glued to
486 the surrounding skull. A custom-made 3D printed titanium head bar was cemented to the skull
487 together with the cannula. Buprenorphine hydrochloride (Bupaq, 0.1 mg/kg) and carprofen
488 (Rimadyl, 25 mg/kg) were administered subcutaneously for analgesia and preventing inflammation.

489 During the 2 days of postoperative care, the animal's drinking water was supplemented with 35
490 ng/ml of carprofen.

491 **Behavioral training**

492 Water-restriction started 24 hours before behavioral training (median: 4, range: 2 - 45 days after
493 surgery). Throughout training days, animals received 5% sucrose solution as a reward during
494 behavioral sessions. If an animal's weight fell below 85% of its starting weight by the end of the
495 training/imaging session, the animal was provided free access to water for 10 minutes in its home
496 cage. On the first day of training animals were habituated to head-fixation in the behavioral setup
497 and were encouraged to run on a virtual reality attached treadmill by receiving rewards via a lick-port
498 at regular intervals. A virtual corridor was displayed on three flat screens placed in front and on the
499 two sides of the animal's head and synchronized with the movement of the treadmill (PyOgre
500 virtual reality and Luigs & Neumann treadmill logged and synchronized via a LabVIEW software).
501 The animal was also rewarded for licking the lick-port in the designated reward zone. Upon reaching
502 the end of the corridor, animals were instantly teleported to the start. On the following days, the
503 distance between running-related rewards was gradually increased until animals relied solely on
504 operant rewards in the reward zone at the end of the corridor. Subsequently, the length of the
505 virtual environment was gradually extended from 2 to ~8 meters by adding new segments to the
506 beginning of the corridor. Animals were trained until they completed at least 50 laps within 30
507 minutes (median = 22, range 11 - 99 days).

508 ***In vivo* two-photon [Ca^{2+}] imaging**

509 Two-photon [Ca^{2+}] imaging of CA1PCs was performed *in vivo* in the CA1 region of the left dorsal
510 hippocampus in well-trained animals running typically 50 laps per session. A Femto-2D dual two-
511 photon microscope equipped with a Nikon LWD 16X objective lens (NA = 0.80) was used and the
512 laser power was set to ~70 mW at the specimen, with a wavelength of 920 nm. Images of 512 by
513 505 pixels were acquired at a frame rate of ~31 Hz with a spatial resolution of 0.89 x 0.89 μm /
514 pixel.

515 **Analysis of *in vivo* [Ca^{2+}] imaging data**

516 Motion correction, ROI detection, fluorescent trace extraction, and neuronal activity deconvolution
517 were performed using the Suite2p software, followed by analysis with custom-written Python scripts.

518 Suite2p-identified ROIs exhibiting unrealistic shapes were excluded from the study based on the
519 consensus of three human experts (JM, ZN, MS) blinded to the fluorescent activity of these ROIs.

520 To account for background fluorescence originating from neuropil (tissue consisting of neuronal
521 and glial processes surrounding the cell bodies), we performed neuropil correction. The corrected
522 fluorescence (F) for each ROI was calculated by subtracting a scaled version (0.7x) of the Suite2p-
523 estimated neuropil fluorescence (F_{neu}) from the raw fluorescence values (F_{raw}): $F = F_{raw} - 0.7 \text{ X } F_{neu}$.
524 For a conservative estimation of inferred neuronal activities, we used the Suite2p spks output
525 containing neuronal activity events deconvolved from the underlying fluorescence traces. We filtered
526 the spks output by the following process. Local noise was assessed around each non-zero spks value.
527 Local maxima of the neuropil-subtracted fluorescence (F) were identified between each non-zero
528 spks value and the following nineth frame. These maxima were replaced with the average value of
529 three neighboring fluorescence data points around the peak (F_{max}). Next, a linear baseline was fit to
530 the fluorescence data points from the -30th to the -20th frame preceding each non-zero spks value.
531 The local noise of the fluorescence (SD_{local}) was calculated as the root-mean-square error (RMSE) of
532 the linear fit. The baseline fluorescence (F_{base}) for each activity was defined as the linear prediction at
533 the -20th frame position. Global noise was characterized by the standard deviation (SD_{global}) of F
534 values within the range 1.5 times below and 0.5 times above the median F value of the entire
535 fluorescence trace. A non-zero spks value was considered valid only if the corresponding
536 fluorescence transient amplitude (F_{max} - F_{base}) exceeded both the local and global noise. The resulting,
537 noise-reduced inferred activity values were used for all subsequent analyses.

538 For comparing the amplitude of [Ca^{2+}] transients in laps before, during and after PFFs, we have also
539 calculated the change in fluorescence relative to baseline ($\Delta F/F$). Each neuropil-corrected
540 fluorescence value was divided by the median of the preceding 1000 fluorescence values. For values
541 earlier than the 1000th time point we used the following 1000 timepoints for median calculation. The
542 neuropil-subtracted $\Delta F/F$ traces from multiple ROIs during PF transitions were aligned, if at least
543 one inferred activity occurred during the transition. The $\Delta F/F$ traces were smoothed using a 5-point
544 wide symmetrical moving average. The difference between each smoothed point and the 4th point
545 before it was then calculated. The position of the maximum in this difference curve, corresponding
546 to the steepest rising phase of the fluorescence transient, was used for trace alignment. For place
547 field transitions without inferred events, the traces were aligned to their midpoint. Following trace
548 alignment, an asymmetrical window encompassing -50 to 150 data points around the alignment

point was isolated. The mean ΔF/F trace within this window across all transitions was calculated, and the position of its maximum determined. The peak amplitude for each trace was then calculated by subtracting the median ΔF/F value of the isolated segment from the ΔF/F value at the maximum of the mean trace. Finally, average and standard deviation of these peak amplitudes were calculated across all traces.

Newly formed PF demarcation and categorization

Spatial demarcation

The 832 cm long virtual environment was discretized into 4.24 cm wide space bins and data from bins with average running speed lower than 4 cm/s were excluded. Odd and even laps were separated and used for calculating mean inferred activity in each spatial bin across laps (odd and even tuning curves). ROIs with smaller than 0.25 Pearson's product-moment correlation coefficient between odd and even tuning curves were excluded from further analysis. We assessed spatial information in each ROI using Skaggs's metric (Skaggs et al., 1992). Statistical significance was assessed using a bootstrapping procedure performed in Python. The inferred activity data for each lap was circularly shifted with a random amount in time and Skaggs's information content was recalculated 1500 times to create a null distribution. ROIs with Skaggs's score exceeding the 99th percentile of the shuffled distribution were selected for further processing (Eliav et al., 2021). Tuning curves for each ROI were calculated as the mean inferred activity in each spatial bin across laps. Peaks and their footprints, the area they cover on the space axis, in the tuning curves were identified using functions from the SciPy library: find_peaks (peak_height = 6), peak_prominences, and peak_widths (rel_height = 0.93). Adjacent peaks were merged if their footprints overlapped or the intervening minimum value between peaks was greater than half the amplitude of the larger peak. Spatial boundaries were calculated as spacebin at the left and right edges of spatial footprints. To identify spatial regions with statistically significant spatial tuning, we employed a localized information metric. First, for each peak identified in the tuning curves, we extended its footprint by half its width in both directions. Within these extended regions, a local Skaggs' information metric was calculated. To assess the significance of this metric, a null distribution was generated using bootstrapping as above (1500 iterations). The inferred activity for the selected region was circularly permuted with a random time shift in each lap, followed by recalculating the Skaggs' information content. The 95th percentile of this null distribution served as the significance criterion to identify

regions exhibiting statistically high spatial location selectivity. Regions with statistically high spatial selectivity were considered as PFs if they had at least one inferred activity in at least 30% of the laps.

Temporal demarcation

To ensure a conservative estimate of PF formation time and avoid misidentification of small neuronal activities or noise as formation events, the inferred activity data below 64 a.u. was set to zero. This step excluded potentially ambiguous neuronal activities that might be difficult to confirm visually in the motion-corrected videos (see in Quality control of signal isolation for BTSP and non-BTSP related place field formations).

For analyzing the formation and end laps of newly formed PFs, we used this thresholded inferred activity data, within the previously identified PF spatial boundaries but without filtering based on running speed of the animal. To account for the potential for place fields to exhibit a backward shift in activity relative to the formation lap, we extended the previously identified spatial boundaries in the forward direction (to the right) by 5 space bins or until the end of the corridor. This approach ensured that formation events occurring at locations forward compared to the place field's spatial center (as expected for BTSP) would be detected. We identified potential PFF events by analyzing the inferred activity data across laps. First, we constructed a PF activity matrix by calculating the average activity for each spatial bin within the PF across all laps. To ensure minimal pre-formation event activity, only laps after the 17th were considered for potential formation events. A lap was classified as a formation lap only if no more than 10% of the previous laps had a mean activity exceeding 1% of the mean activity of the potential formation lap. In maze extension experiments (Figure 4), the minimum 17 pre-formation laps requirement was ignored. A PF was considered to be terminated if at least five consecutive laps with no activity occurred or the final lap of the session was reached.

Categorization of newly formed PFs

We employed a three-step process to categorize newly formed PFs. First, we excluded PFs that were formed in the first 17 laps. Second, we excluded PFs that exhibited a lifetime < 9 laps. Finally, we addressed activity consistency within PFs. Lap-wise maximum activity rates of the PF activity matrix were normalized to the peak activity rate across all laps. Place fields were excluded if the number of silent laps (laps with normalized activity below 10%) exceeded 8 laps. Place fields were categorized as showing formation lap gain if the peak activity value in the formation lap was greater than the

609 average peak activity value observed across the subsequent three active laps. For further
610 categorization of the newly formed PFs, the center of mass (COM) was calculated for each active
611 lap and smoothed across laps using a running average with a kernel size of 3. The formation point
612 of the PF was defined as the activity COM in the formation lap. Finally, the mean COM value for
613 the first three post formation active laps was calculated. If this mean value was smaller than the
614 formation point, the PF was categorized as exhibiting an initial backward shift. To exclude
615 misinterpretation of occasionally observed continuous drift of the PF COM as BTSP-like initial
616 shift, we also quantified continuous backward drift (termed 'drift') in the PF. For this, we first
617 isolated the smoothed COM values for each lap, starting from the fourth active lap after the
618 formation. We then performed a linear regression analysis on these COM value series. If the
619 calculated COM value in the first lap after formation lap extrapolated from the regression line was
620 not larger than the formation points or the Spearman's rank correlation coefficient between the
621 COM values and their sequential labels was not statistically significant ($p < 0.05$) with a negative
622 value, we categorized the PF as lacking significant drift.

623 We categorized PF formation events based on their activity patterns during and after formation.
624 PFFs were considered BTSP-like if they fulfilled all of the following criteria: 1) showed formation
625 lap gain, 2) followed by a backward shift in the place representation, and 3) showed no significant
626 further drift. Conversely, PFFs that lacked both 1) formation lap gain and 2) an initial backward shift
627 during formation, regardless of the PFs' drift characteristics, were classified as non-BTSP-like. In
628 our initial categorization we found 808 candidate BTSP-like and 165 non-BTSP-like PFFs, which
629 were further analyzed as detailed below. An additional 560 PFs could not be included in the above
630 two groups (238 PFs with formation lap gain but without backward shift; 312 PFs with no
631 formation lap gain but with backward shift); these PFs were excluded from further analysis in this
632 study.

633 We emphasize that we employed a conservative approach for categorizing PFFs: we only included
634 PFF events in our analysis if they fulfilled all criteria of either BTSP-like or non-BTSP-like groups
635 and excluded PFFs that failed on at least one criterion. Yet, it should be noted that BTSP might
636 occur without positive gain (if the cell fires CSBs in the PF on multiple laps after the formation lap)
637 as well as without negative shift (since the plasticity kernel extends over zero to positive timings as
638 well). In addition, the nonlinear relationship between electrical activity and [Ca^{2+}] signals, as well as
639 the lack of sensitivity of GCaMP6s to detect single APs, may add uncertainty to our classification.

640 **Quality control of signal isolation for BTSP and non-BTSP related PF formations**

641 Automated ROI segmentation by Suite2p can encompass processes from multiple cells which can
642 lead to erroneously reported [Ca^{2+}] dynamics during PF activity. To address this and facilitate human
643 confirmation of automated ROI segmentation, we isolated short motion corrected video segments
644 from place cells and their surroundings exhibiting BTSP- (n = 808) and non-BTSP-like (n = 165)
645 PFFs. To quantify the spatial footprints of active neurons during the animal's PF transitions, we
646 employed a method to assess local coherence of fluorescence signals within the field of view. For
647 each pixel in an isolated video frame, we assigned an intensity by averaging the Pearson's product-
648 moment correlation coefficients between its time series and the time series of its eight nearest
649 neighbors. In the resultant grayscale image, pixels corresponding to active cells were given higher
650 intensity values, reflecting the synchronized activation of these pixels during neuronal spiking. The
651 contrast of the resulting grayscale image was further enhanced with Scikit-image's
652 exposure.adjust_sigmoid function (cutoff = 0.8, gain = 20). Finally, to incorporate the temporal
653 aspect of pixel activation patterns, we applied a pseudo-color map. This map assigned a color to
654 each pixel based on the center of mass of its intensity time series. In essence, these spatial footprints
655 showed the shape of active cells with their subregions colored based on their average timing of
656 activity. The spatial footprints of each PF transition were visually inspected and ROIs with
657 multicolored subregions were excluded. All motion corrected video segments for the remaining
658 ROIs were visually inspected.

659 **Detection of solitary [Ca^{2+}] transients**

660 Solitary [Ca^{2+}] transients were identified by the following process. First, for each BTSP-like PFF
661 event, we calculated the maximum $\Delta F/F$ value by analyzing timepoints recorded during the animal's
662 traversal across the width of the PF in the formation lap extended by 5 space bins to the right but
663 not further than the end of the corridor. This maximum amplitude served as the parameter for peak
664 detection (Scipy, 'find_peaks', prominence = 1, distance = 20) to identify peaks equal to or larger
665 than this formation lap peak amplitude. Second, [Ca^{2+}] transients within the spatial boundaries of
666 any existing or newly formed PFs were excluded. To further ensure that the detected solitary peak
667 wasn't part of a short-lived place modulated activity, we calculated the maximum $\Delta F/F$ value from
668 the previous and following 5 laps within 11 spatial bins centered around the peak containing space
669 bin. If the maximum $\Delta F/F$ in this area exceeded the median plus two SD of the ROIs' $\Delta F/F$ values
670 from the entire session, the solitary event was excluded. For each ROIs only the largest solitary peak

was used for calculating the mean waveform, but we note that in many cells multiple [Ca^{2+}] transients in a given session fulfilled the criteria for solitary events.

Lap-by-lap population vector correlations

For each Suite2p ROI, the non-thresholded inferred activity data collected during each space bin transition was averaged. Subsequently, Pearson correlation coefficients were calculated between the mean activity of the ROIs at each spatial location for every possible lap pair. Finally, the lap-by-lap PV correlation for a given lap pair was determined by averaging these location-specific correlation coefficients.

Odd-even lap population vector correlations

To evaluate population-wide activity changes upon the extension of the familiar corridor by a new maze segment, we computed population vector correlations between odd and even laps for the first 6 meters of the familiar pre-extension maze (excluding the reward zone) and the 6-meter-long new extension part of the maze. For each ROI, we first calculated the mean non-thresholded inferred activity from each spatial bin for both odd and even laps from the session immediately preceding novel maze segment insertion and during the extended maze experiment. These population vectors were then used to calculate the average pairwise Pearson correlations between intra-corridor and cross-corridor odd-even lap data for each animal. Finally, we compared the means of these correlations across animals for both intra-corridor and cross-corridor population vector correlations.

Statistics

Statistical analyses were performed using Statistica (General Linear Model with repeated measures or mixed ANOVA; software version 14.0.1.25, Tibco) or Python (correlations, bootstrapping). Tukey's test was applied for *post hoc* comparisons after a significant effect was demonstrated by the main ANOVA.

695 **Figure legends:**

696 **Figure. 1 *In vivo* two-photon [Ca^{2+}] imaging from head restrained mice during spatial**
697 **navigation in a virtual corridor**

698 (A) Double transgenic mice (GCaMP6s and Cre-dependent td-Tomato) were injected with a diluted
699 AAV expressing Cre-recombinase for sparse td-Tomato labelling. Following craniotomy and cannula
700 implantation above the left dorsal CA1 area, animals were trained and imaged with a two-photon
701 (2P) microscope during navigation in an ~8-meter-long virtual corridor. Timeline shows the
702 minimum, (median), and maximum number of days between the procedures.

703 (B) Mean 2P image of an imaging field of view. Example cells shown in panel (E), (G) and (I) are
704 indicated by colored circles.

705 (C) Wall pattern of the virtual corridor consisting of low contrast random checkerboard background
706 with 6 high contrast vertical visual landmarks.

707 (D) Average running speed (orange: mean; ± SD: grey) decreased and lick propensity (blue)
708 increased before the animal reached the reward zone (green area).

709 (E) ROI masks and [Ca^{2+}] signals during a single session of the cells marked in panel (B). Gray
710 segments correspond to odd laps in the virtual environment.

711 (F) Position of the animal along the corridor aligned with the fluorescence activity shown in panel
712 (E).

713 (G, H) Same as panel (E) and (F) on an extended time scale showing a single lap (indicated by * in
714 (E)). Time periods when the animals' running speed was below 5 cm/s are shown in red and were
715 excluded from the analysis. Black vertical bars are inferred activity.

716 (I) Raster plots showing the inferred neuronal activity of three cells (color coded cells in panel (B),
717 (E) and (G)) as a function of the lap number and spatial location of the animal.

718 (J) Coverage of the virtual corridors by place fields (PFs). Tuning curves from cells with at least one
719 significant PF are included. The tuning curves are ordered by the location of their largest peak
720 activity. Left panel: Data from a single session. Right panel: Data from all experiments (22,325 place
721 cells recorded across 163 sessions from 45 mice) was randomly down sampled to match the sample
722 size of the single run.

723 (K) Distributions of the number of PFs of place cells, PF widths, and PF coverage of the virtual
724 corridor. Data are presented for all sessions and for a single session (insets).

725

726 **Figure 2. Comparison of [Ca^{2+}] transients underlying different place field formation events**

727 (A) BTSP-like PFFs. Activity raster plots (left) show three example cells with BTSP-like PFFs (red
728 arrows). The middle panels display the isolated activity of newly formed PFs marked by red arrows.
729 Fluorescence traces (right) are shown before, during (red traces), and after PFF (± 5 laps).

730 (B) Same as (A), but for non-BTSP-like PFFs (blue arrows and traces).

731 (C) Comparison of [Ca^{2+}] transients before, during, and after PFF. Fluorescence traces for BTSP-
732 (left) and non-BTSP-like (right) PFFs are shown for each lap spanning from the pre-formation lap
733 (FL-1) to the fourth lap after formation (FL+4). Traces were aligned to the midpoint of the steepest
734 rising slope for detectable [Ca^{2+}] transients, or to the timepoint at which the place field center was
735 reached for traces lacking transients. The mean fluorescent transients are shown in red for BTSP and
736 blue for non-BTSP-like events. Insets: Peak-normalized and peak-aligned mean fluorescence traces
737 are superimposed. Bar graphs depict the mean raw fluorescence activity (± SD, BTSP: n = 310
738 events, non-BTSP: n = 59 events from 30 mice) in the given lap. Statistical analysis revealed that the
739 amplitude of the [Ca^{2+}] transients in the formation lap is significantly higher for the BTSP compared
740 to the non-BTSP-like events and the amplitudes in the other laps are not significantly different
741 (Mixed ANOVA: main effect for group (BTSP/non-BTSP): $p = 0.033$; lap: $p < 0.001$, interaction: p
742 < 0.001; Tukey *post hoc* test: formation lap: $p < 0.001$, all other laps: $p > 0.787$).

743

744 **Figure 3. Newly formed place fields cover the entire virtual corridor and have non-uniform**
745 **birth rates**

746 (A) The tuning curves of BTSP- (left) and non-BTSP-like (right) PFs were ordered by the center
747 position of their newly born PFs (white space bins).

748 (B) The width of BTSP-like newly formed PFs is correlated with the animal's running speed during
749 PFF. Scatter plot shows individual BTSP- (red symbols) and non-BTSP-like (blue symbols) PFF
750 events (Spearman correlations: BTSP: $R = 0.40$, $p = 3.4 \times 10^{-13}$; non-BTSP: $R = 0.15$, $p = 0.25$).

751 (C) Histogram of the number of newly formed PFs per single session in the virtual corridor. Note
752 that a few sessions have unusually high (>20) new PFF events.

753 (D) Number of newly formed PFs by laps. Example sessions showing high number of BTSP- (red)
754 and non-BTSP-like (blue) PFFs (upper panels, two of the largest three sessions of the histogram in
755 panel (C)) and sessions with moderate number of PF formations (lower panels). The histograms are
756 aligned with lap-by-lap population vector correlograms, which reveal sudden change in population
757 activity for the upper panels and lack of such representational switch for the lower panels.

758 (E) [Ca^{2+}] transients of PFF events during representational switches (switch, isolated from sessions
759 with the three highest number of PFF event in the histogram in panel (C)) are compared to PFF
760 events outside representational switches (no switch) for BTSP- (left) and non-BTSP-like (right)
761 events. Fluorescence traces are shown from the lap preceding PFF (FL-1) to the lap following PFF
762 (FL+1). Traces were aligned to the midpoint of the steepest rising slope, or to the timepoint at
763 which the PF center was reached (for traces without detectable transients). The mean traces are
764 shown in orange, red, cyan and blue. Insets: peak-normalized and peak-aligned mean fluorescence
765 traces. Bar graphs depict the peak of the mean fluorescence waveform (mean ± SD; BTSP no
766 switch: $n = 270$, BTSP switch: $n = 40$, non-BTSP no switch: $n = 36$, non-BTSP switch: $n = 23$
767 events from 30 mice) in the given lap. The peak amplitudes of [Ca^{2+}] transients are not significantly
768 different for the BTSP-like events (Mixed ANOVA: main effect for group (switch/no switch): $p =$
769 0.463; lap: $p < 0.001$, interaction: $p = 0.256$) and for the formation lap of the non-BTSP-like events
770 but are significantly higher for non-BTSP-like events during switches than outside switches in the lap
771 after the formation lap (Mixed ANOVA: main effect for group (switch/no switch): $p = 0.001$; lap: p
772 < 0.001, interaction: $p < 0.001$; Tukey's *post hoc* test: formation lap -1: $p = 0.999$, formation lap: $p =$
773 0.847, formation lap+1: $p < 0.001$).

774

775 **Figure 4. Similar [Ca^{2+}] transients underlie place field formation in familiar and novel**
776 **environments**

777 (A) Place field formation (PFF) in a familiar environment with a novel extension. A familiar corridor
778 was extended with a new 6-m-long segment. New PFs appear already during the first traversal (top)
779 by both BTSP- (red arrow) and non-BTSP-like (blue arrow) dynamics. Bottom, fluorescence [Ca^{2+}]
780 transients during and after the PFFs marked on the raster plot.

781 (B) Histogram of BTSP- and non-BTSP-like PFFs during the first session in the extended maze
782 region (n = 6 mice).

783 (C) [Ca^{2+}] transients of the formation lap and the following lap (FL+1) of BTSP- (left panels) and
784 non-BTSP-like (right panels) PFF events in the new extension. The mean fluorescent activities of
785 BTSP- (red) and non-BTSP-like (blue) PFFs are also displayed. Insets show peak-normalized, peak-
786 aligned mean fluorescence traces. Bar graphs show the mean fluorescence activities (peak amplitude
787 ± SD) during initial encounter ($BTSP_{NEW}$, red, n = 24, non-$BTSP_{NEW}$: blue, n = 16 events) of the
788 novel environment (n = 6 animals), and familiar environment (BTSP- and non-BTSP: black; data
789 from Figure 2). The amplitudes of [Ca^{2+}] transients in the formation lap and the lap after formation
790 were not significantly different between the new and familiar environments for both BTSP- and
791 non-BTSP-like events (two-way mixed ANOVA: main effect for PFF type (BTSP/non-BTSP): $p <$
792 0.001, corridor (familiar/new): $p = 0.996$, type vs. corridor: $p = 0.226$, lap: $p < 0.026$, lap vs type: p
793 < 0.001, lap vs. corridor: $P = 0.692$, lap vs. type vs. corridor: $p = 0.049$; Tukey *post hoc* tests: lap0:
794 BTSP new vs. familiar: $p = 0.999$, non-BTSP new vs. familiar: $p = 1$; lap1: BTSP new vs. familiar: p
795 $= 0.540$, non-BTSP new vs. familiar: $p = 0.939$).

796

797 **Figure 5. Large somatic [Ca^{2+}] events are often not sufficient to evoke novel place field**

798 (A) Raster plots of neuronal activity (top) and [Ca^{2+}] transients (bottom) vs. spatial location vs. laps
799 for three example cells reveal BTSP-like new PFFs (red arrows) as well as large amplitude activities
800 (magenta arrows) which did not evoke new PFs (solitary events).

801 (B) Fluorescence traces around the same BTSP-like PFF events (red) marked in panel (A) and larger
802 amplitude [Ca^{2+}] transients not associated with PFF (magenta) within the same sessions are shown.

803 (C) Trace pairs from the lap before (EL-1), during (Event Lap) and the lap after (EL+1) for BTSP-
804 like PFF events (left traces) and solitary non-PF yielding events (right traces) identified within a
805 session. In EL-1, traces were aligned to the timepoint of crossing the center of the PF. Pre and post
806 solitary event traces were aligned to the crossing time of the first space bin of the corresponding
807 solitary event. Inset: peak-normalized and peak-aligned mean fluorescence traces. Bar graphs depict
808 the peak amplitudes of [Ca^{2+}] transients (mean ± SD; BTSP: n = 60, solitary: n = 60 events, n = 23
809 mice) in the given laps. The amplitudes of [Ca^{2+}] transients of the solitary events in the event lap
810 were significantly higher, whereas in the EL+1 they were smaller compared to those of BTSP-like

events (Mixed ANOVA: main effect for group (BTSP/solitary): $p = 0.681$, lap: $p < 0.001$, interaction: $p < 0.001$; Tukey *post hoc* test: lap -1: $p = 0.999$, event lap: $p < 0.001$, lap+1: $p < 0.001$).

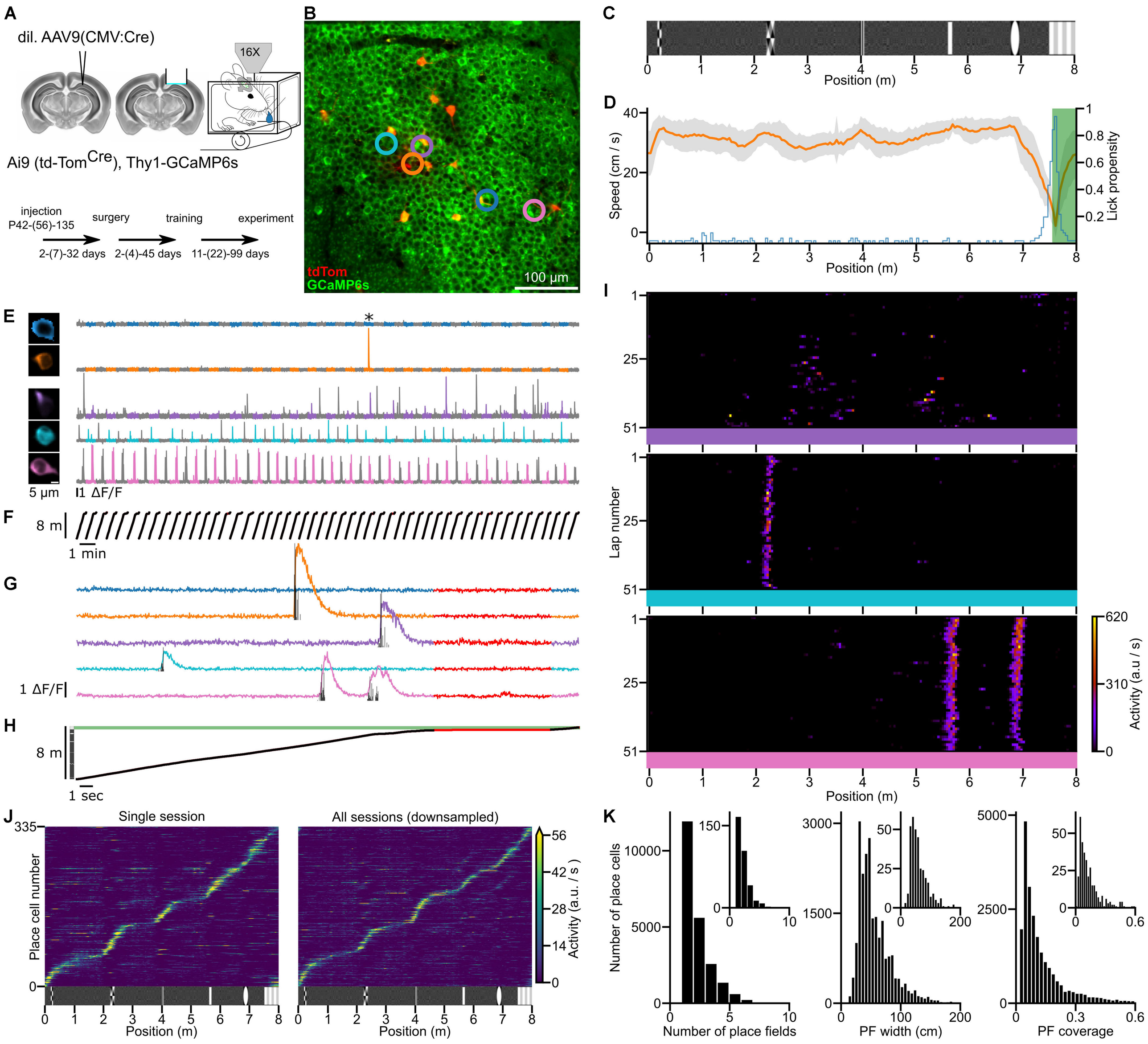
A
dil. AAV9(CMV:Cre)
16X
Ai9 (td-Tom^Cre), Thy1-GCaMP6s
injection P42-(56)-135
surgery
training
experiment
2-(7)-32 days
2-(4)-45 days
11-(22)-99 days
B
tdTom
GCaMP6s
100 µm
C
Position (m)
D
Speed (cm / s)
Lick propensity
Position (m)
E
5 µm
1 ΔF/F
F
8 m
1 min
G
1 ΔF/F
H
8 m
1 sec
I
Lap number
Activity (a.u / s)
Position (m)
J
Single session
All sessions (downsampled)
Place cell number
Activity (a.u. / s)
Position (m)
K
Number of place cells
Number of place fields
PF width (cm)
PF coverage

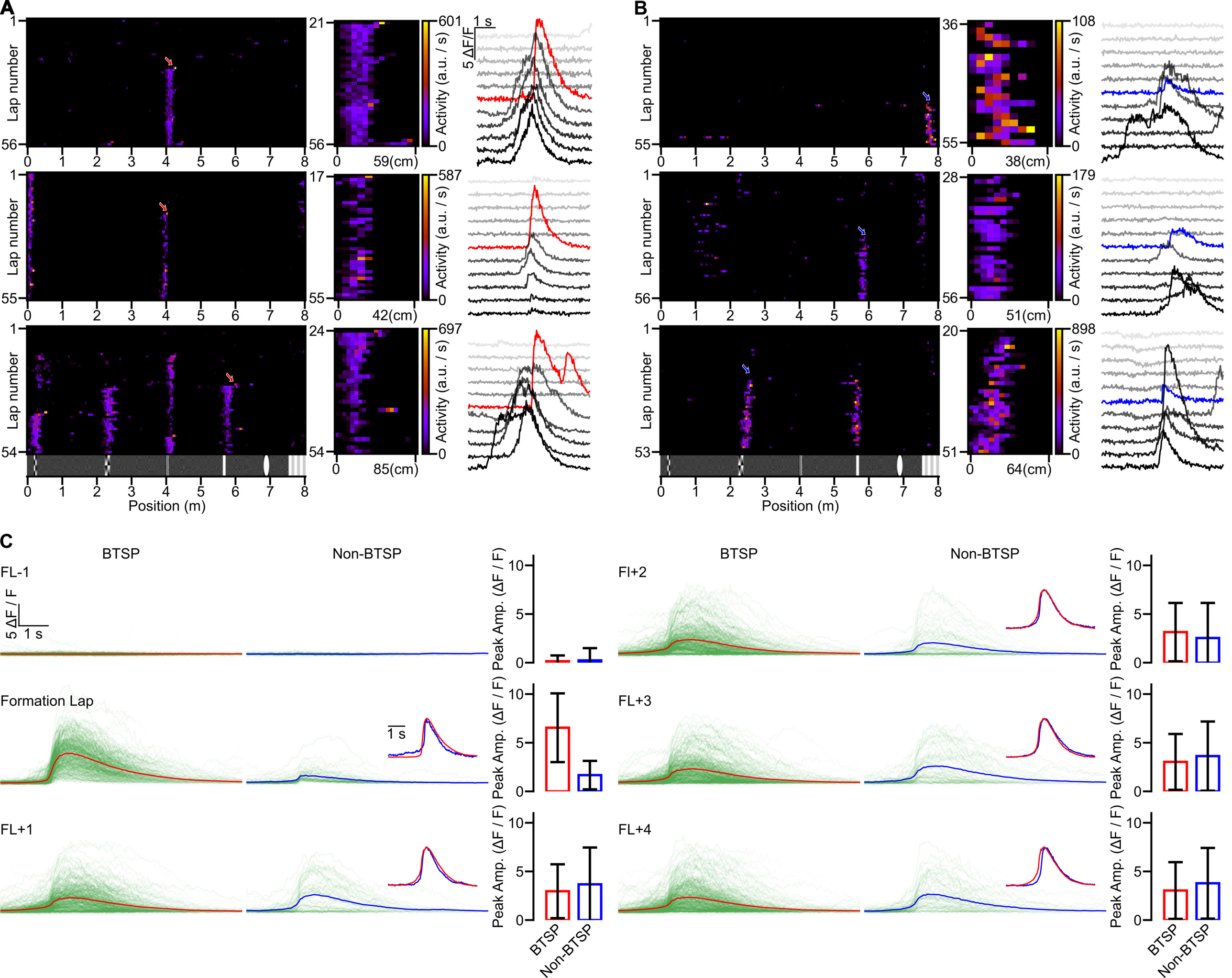
A
B
C
Lap number
Activity (a.u. / s)
Position (m)
59(cm)
42(cm)
85(cm)
38(cm)
51(cm)
64(cm)
1 s
5 ΔF/F
BTSP
Non-BTSP
FL-1
Formation Lap
FL+1
Fl+2
FL+3
FL+4
5 ΔF / F
Peak Amp. (ΔF / F)

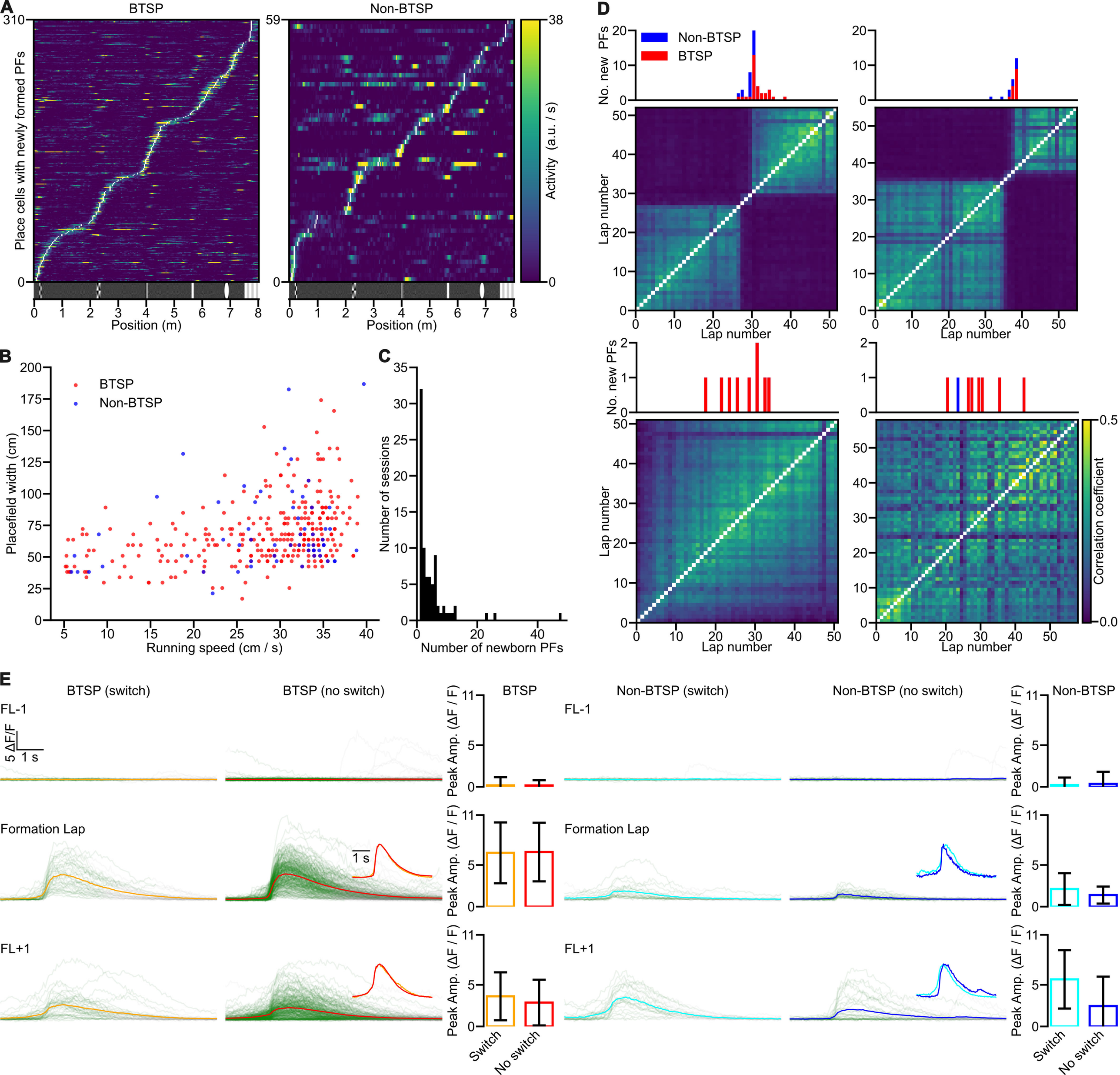
A
BTSP
Non-BTSP
Place cells with newly formed PFs
Position (m)
Activity (a.u. / s)
B
BTSP
Non-BTSP
Placefield width (cm)
Running speed (cm / s)
C
Number of sessions
Number of newborn PFs
D
Non-BTSP
BTSP
No. new PFs
Lap number
Correlation coefficient
E
BTSP (switch)
BTSP (no switch)
BTSP
Non-BTSP (switch)
Non-BTSP (no switch)
Non-BTSP
FL-1
Formation Lap
FL+1
5 ΔF/F
1 s
Peak Amp. (ΔF / F)
Switch
No switch

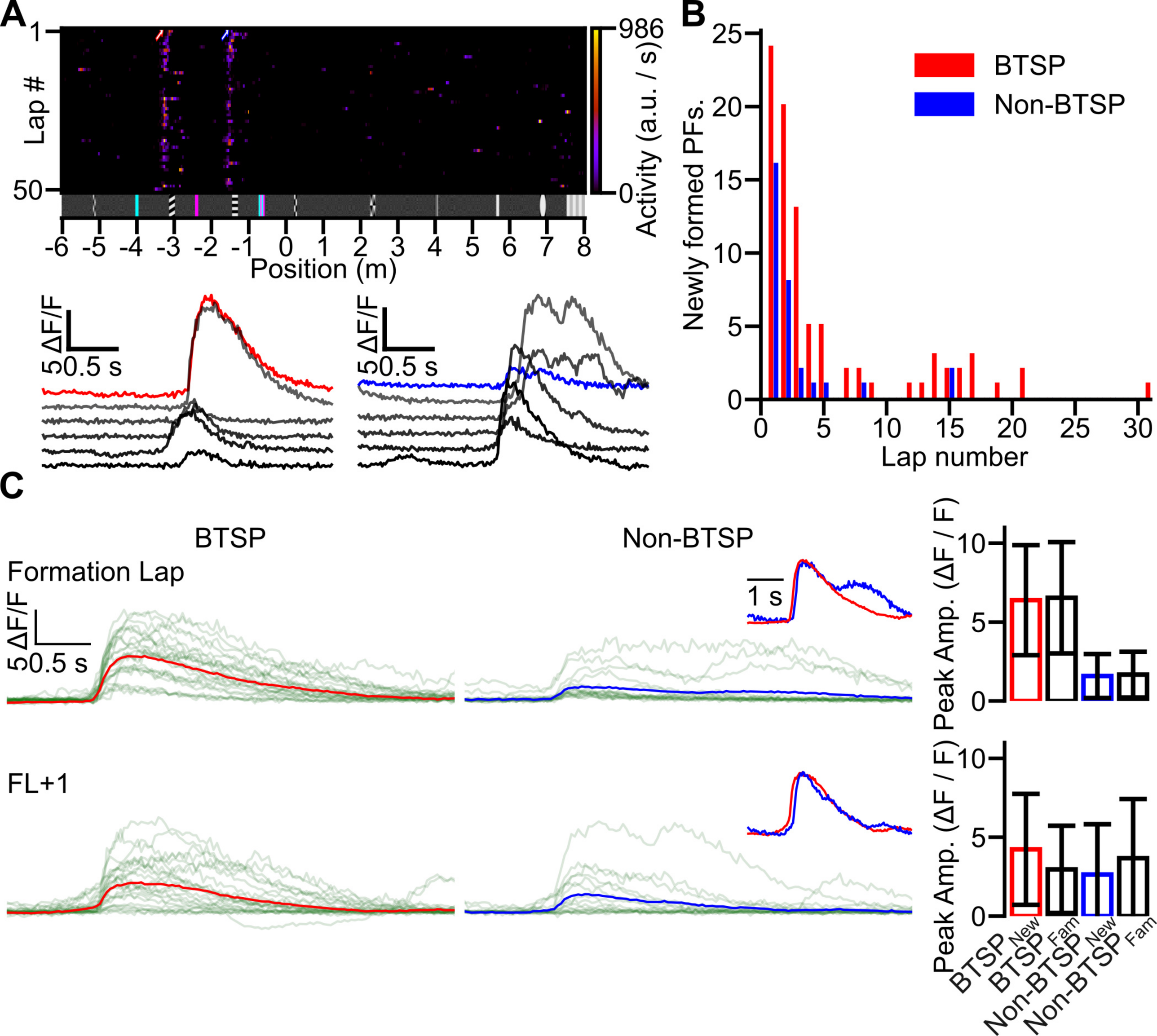
A
Lap #
1
50
986
0
Activity (a.u. / s)
-6 -5 -4 -3 -2 -1 0 1 2 3 4 5 6 7 8
Position (m)
5 ΔF/F
0.5 s
5 ΔF/F
0.5 s
B
BTSP
Non-BTSP
Newly formed PFs.
0 5 10 15 20 25
0 5 10 15 20 25 30
Lap number
C
BTSP
Non-BTSP
Formation Lap
5 ΔF/F
0.5 s
1 s
FL+1
Peak Amp. (ΔF / F)
0 5 10
BTSP New
BTSP Fam
Non-BTSP New
Non-BTSP Fam

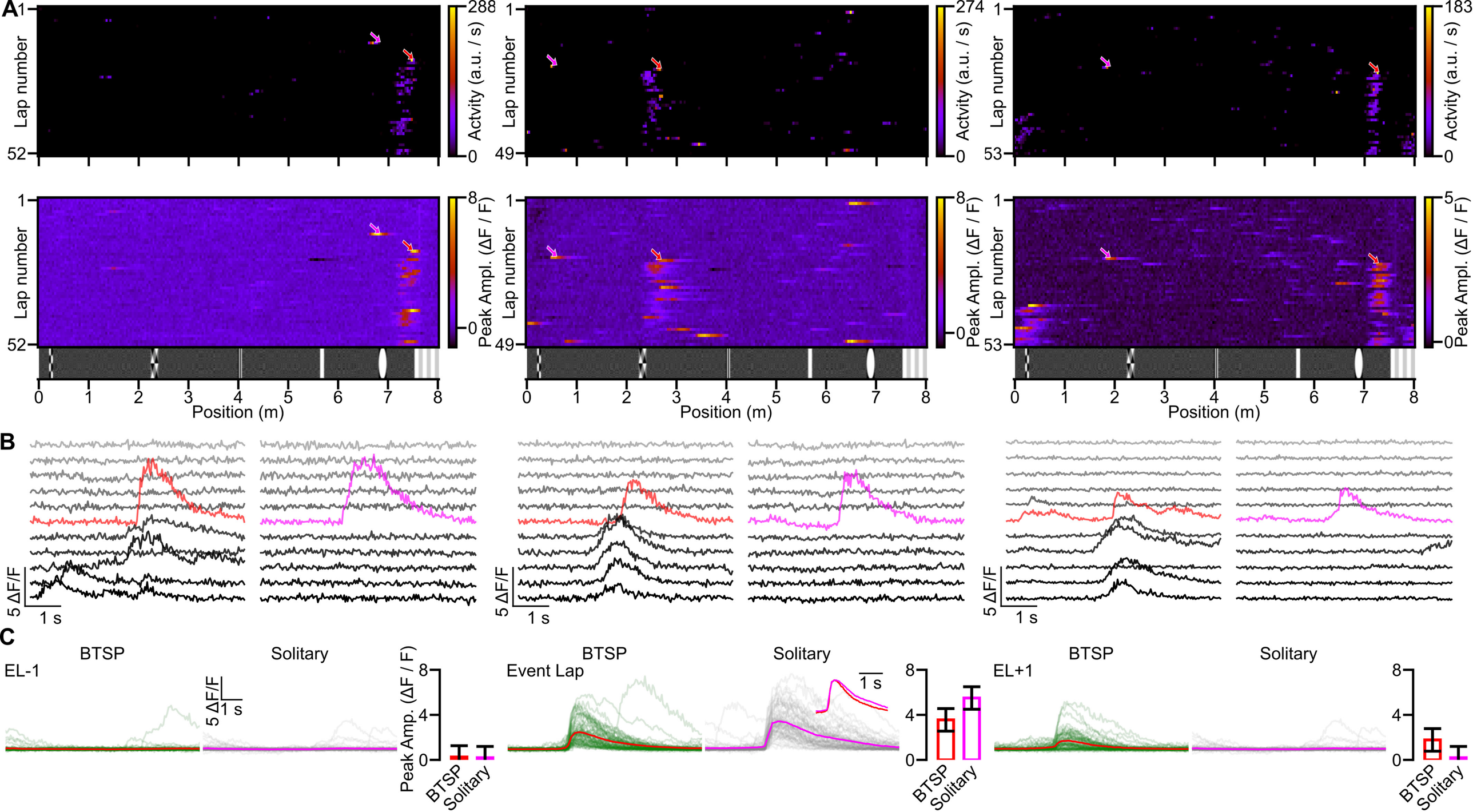
A
Lap number
Activity (a.u. / s)
Peak Ampl. (ΔF / F)
Position (m)
B
5 ΔF/F
1 s
C
BTSP
Solitary
EL-1
Event Lap
EL+1
Peak Amp. (ΔF / F)